Statistical intensity correction and segmentation of MRI data

W. M. Wells III * W.E.L. Grimson † R. Kikinis ‡ F. A. Jolesz §

1 ABSTRACT

Many applications of MRI are facilitated by segmenting the volume spanned by the imagery into the various tissue types that are present. Intensity-based classification of MR images has proven to be problematic, even when advanced techniques such as non-parametric multi-channel methods are used. A persistent difficulty has been accommodating the spatial intensity inhomogeneities that are due to the equipment.

This paper describes a statistical method that uses knowledge of tissue properties and intensity inhomogeneities to correct for these intensity inhomogeneities. Use of the Expectation-Maximization algorithm leads to a method (EM segmentation) for simultaneously estimating tissue class and the correcting gain field. The algorithm iterates two components to convergence: tissue classification, and gain field estimation. The result is a powerful new technique for segmenting and correcting MR images.

An implementation of the method is discussed, and results are reported for segmentation of white matter and gray matter in gradient-echo and spin-echo images. Examples are shown for axial, coronal and sagittal (surface coil) images. For a given type of acquisition, intensity variations across patients, scans, and equipment have been accommodated without manual intervention in the segmentation. In this sense, the method is fully automatic for segmenting healthy brain tissue.

An accuracy assessment was made in which the method was compared to manual segmentation, and to a method based on supervised multi-variate classification, in segmenting white matter and gray matter. The method was found to be consistent with manual segmentation, and closer to manual segmentation than the supervised method.

2 INTRODUCTION

Magnetic resonance imaging (MRI) provides rich information about anatomical structure, enabling quantitative anatomical studies [1]; the derivation of computerized anatomical atlases [2]; as well as 3D visualization of internal anatomy, for use in pre- and intra-operative visualization [3], and in the guidance of therapeutic intervention .

Applications that use the structural contents of MRI are facilitated by segmenting the imaged volume into tissue types. Such tissue segmentation is often achieved by applying statistical classification methods to the signal intensities [4 5] , in conjunction with morphological image processing operations [6 7].

Intensity-based classification of MR images has proven problematic, however, even when advanced techniques such as non-parametric multi-channel methods are used, primarily due to spatial intensity inhomogeneities that are due to the equipment. The MRI signal is derived from radio-frequency (RF) signals emanating from the scanned tissues. Diagnostic MRI machines frequently use RF coils (antennae) that are designed to have uniform RF sensitivity throughout their working volume. Although images derived from such coils appear visually uniform, there are often significant departures from the ideal that disturb intensity-based segmentation methods. For example, when differentiating between white matter and gray matter in the brain, the spatial intensity inhomogeneities are often of sufficient magnitude to cause the distributions of intensities associated with these two tissue classes to overlap, thereby defeating intensity-based classification.

* Harvard Medical School and Brigham and Women's Hospital, Department of Radiology, 75 Francis St., Boston, MA 02115, sw@ai.mit.edu

† Massachusetts Institute of Technology, Artificial Intelligence Laboratory, 545 Technology Square, Cambridge, MA 02139, welg@ai.mit.edu

‡ Harvard Medical School and Brigham and Women's Hospital, Department of Radiology, 75 Francis St., Boston, MA 02115, kikinis@bwh.harvard.edu

§ Harvard Medical School and Brigham and Women's Hospital, Department of Radiology, 75 Francis St., Boston, MA 02115

This paper describes a statistical method (EM segmentation) that uses knowledge of tissue properties and intensity inhomogeneities to correct for the intensity inhomogeneities of MR images. The result is a method that allows for more accurate segmentation of tissue types as well as better visualization of MRI data.

3 DESCRIPTION OF METHOD

The MRI intensity inhomogeneities addressed in this paper are modelled by a spatially-varying factor called the *gain field* that multiplies the intensity data. Application of a logarithmic transformation to the data allows the artifact to be modeled as an additive *bias* field.

If the gain field is known, then it is relatively easy to estimate tissue class by applying a conventional segmenter to the corrected data. Similarly, if the tissue class is known, then it is straightforward to estimate the gain field by comparing predicted intensities and observed intensities.

It is problematic, however, to determine either the gain or the tissue type without knowledge of the other. The strategy used by EM segmentation is to cycle between estimating the tissue type and the gain throughout the image.

To solve this problem, we first model the bias field, then develop an algorithm that solves for that field, while simultaneously estimating the tissue classifications.

3.1 Bias field estimator

In this section we describe a Bayesian approach to estimating the bias field that represents the gain artifact in log-transformed intensity data. Similar to other approaches to intensity-based segmentation of MRI [6 7], the distribution for observed values is modeled as a normal distribution:

$$p(Y_i \mid \Gamma_i, \beta_i) = \mathrm{G}_\sigma(Y_i - \mu(\Gamma_i) - \beta_i) \quad , \tag{1}$$

where

$$\mathrm{G}_\sigma(x) \equiv \frac{1}{\sqrt{2\pi}\sigma} \exp\left(-\frac{1}{2}\left(\frac{x}{\sigma}\right)^2\right)$$

is the scalar Gaussian distribution, with variance σ^2 and where

Y_i	is the observed intensity at the i^{th} voxel[1]
Γ_i	is the tissue class at the i^{th} voxel[2]
$\mu(x)$	is the mean intensity for tissue class x
β_i	is the bias field at the i^{th} voxel.

A stationary prior (before the image data is seen) probability distribution on tissue class is used, it is denoted

$$p(\Gamma_i) \quad . \tag{2}$$

If this probability is uniform over tissue classes ($p(\Gamma_i) = p \;\forall i$) , our method devolves to a maximum-likelihood approach to the tissue classification component. A spatially-varying prior probability density on brain tissue class is described in [8]. Such a model could profitably be used within our framework.

The entire bias field is denoted by $\beta = (\beta_0, \beta_1, \ldots, \beta_{n-1})^T$. It is modeled by a zero mean Gaussian prior probability density,

$$p(\beta) = \mathrm{G}_{\psi_\beta}(\beta) \quad , \tag{3}$$

where

$$\mathrm{G}_{\psi_\beta}(x) = (2\pi)^{-\frac{n}{2}} |\psi_\beta|^{-\frac{1}{2}} \exp\left(-\frac{1}{2} x^T \psi_\beta^{-1} x\right)$$

is the n-dimensional Gaussian distribution. ψ_β is the $n \times n$ covariance matrix for the entire bias field. We use this model to characterize the spatial smoothness inherent in the bias field.

Using the definition of conditional probability, assuming independence of tissue class and the bias field, and assuming independence of voxels, Bayes rule yields the posterior probability on the bias field, given observations,

$$p(\beta \mid Y) = \prod_i \left[\sum_{\Gamma_i} p\left(Y_i \mid \Gamma_i, \beta_i\right) p\left(\Gamma_i\right)\right] \frac{p(\beta)}{p(Y)} \quad . \tag{4}$$

[1] The extension to vector measurements per voxel is straightforward.

[2] For example, when segmenting brain tissue $\Gamma_i \in \{\mathit{white\text{-}matter}, \mathit{gray\text{-}matter}\}$.

The maximum-a-posteriori (MAP) principle can be used to formulate an estimate of the bias field as the value of β having the largest posterior probability,

$$\hat{\beta} = \arg\max_{\beta} p(\beta \mid Y) \quad . \tag{5}$$

A necessary condition for a maximum of the posterior probability of β is that its gradient with respect to β be zero at the maximum:

$$\left[\frac{\partial}{\partial_{\beta_i}} \ln p(\beta \mid Y) \right]_{\beta = \hat{\beta}} = 0 \qquad \forall_i \quad .$$

Installing the statistical modeling of Equations 1-5 yields the following expression for the zero gradient condition:

$$\left[\frac{\sum_{\Gamma_i} p(\Gamma_i) \, \frac{\partial}{\partial_{\beta_i}} p(Y_i \mid \Gamma_i, \beta_i)}{\sum_{\Gamma_i} p(\Gamma_i) \, p(Y_i \mid \Gamma_i, \beta_i)} + \frac{\frac{\partial}{\partial_{\beta_i}} p(\beta)}{p(\beta)} \right]_{\beta = \hat{\beta}} = 0 \qquad \forall_i \quad .$$

Differentiating the (normal) PDF in the first term yields

$$\left[\frac{\sum_{\Gamma_i} p(\Gamma_i) \, \frac{1}{\sigma^2} (Y_i - \mu(\Gamma_i) - \beta_i) p(Y_i \mid \Gamma_i, \beta_i)}{\sum_{\Gamma_i} p(\Gamma_i) \, p(Y_i \mid \Gamma_i, \beta_i)} + \frac{\frac{\partial}{\partial_{\beta_i}} p(\beta)}{p(\beta)} \right]_{\beta = \hat{\beta}} = 0 \qquad \forall_i \quad .$$

or

$$\left[Y_i - \beta_i - \sum_j W_{ij} \mu(\Gamma_j) + \sigma^2 \frac{\frac{\partial}{\partial_{\beta_i}} p(\beta)}{p(\beta)} \right]_{\beta = \hat{\beta}} = 0 \qquad \forall_i \quad .$$

where

$$W_{ij} \equiv \frac{p(\Gamma_i = \textit{tissue-class-j}) p(Y_i \mid \Gamma_i = \textit{tissue-class-j}, \beta_i)}{\sum_{\Gamma_i} p(\Gamma_i) \, p(Y_i \mid \Gamma_i, \beta_i)} \quad ,$$

or

$$W_{ij} = \frac{p(\Gamma_i = \textit{tissue-class-j}) \mathrm{G}_\sigma (Y_i - \mu(\textit{tissue-class-j}) - \beta_i)}{\sum_{\Gamma_i} p(\Gamma_i) \, \mathrm{G}_\sigma (Y_i - \mu(\Gamma_i) - \beta_i)} \quad . \tag{6}$$

The zero-gradient condition may be re-expressed in matrix notation as follows:

$$\left[Y - \beta - WU + \sigma^2 \frac{\nabla_\beta p(\beta)}{p(\beta)} \right]_{\beta = \hat{\beta}} = \mathbf{0} \quad , \tag{7}$$

where

$$U \equiv (\mu(\textit{tissue-class-1}), \mu(\textit{tissue-class-2}), \ldots)^T$$

is a vector containing the tissue class mean intensities.
Now differentiating the last term of Equation 7 yields

$$\left[Y - \beta - WU - \sigma^2 \psi_\beta^{-1} \beta \right]_{\beta = \hat{\beta}} = \mathbf{0} \quad ,$$

or

$$\left[\beta = H(Y - WU) \right]_{\beta = \hat{\beta}} \quad , \tag{8}$$

where

$$H \equiv (I + \sigma^2 \psi_\beta^{-1})^{-1} \quad . \tag{9}$$

Equation 8 has the superficial appearance of being a linear estimator of the bias field β, given the observations Y. Unfortunately, it isn't a linear estimator, owing to the fact that W (the "weights") are non-linear functions of β (Equation 6).

The result of the statistical modeling in this section has been to formulate the problem of estimating the bias field as a non-linear optimization problem embodied in Equation 8. In the next section an approach to obtaining solutions (estimates) is described.

3.2 EM algorithm

We use the Expectation-Maximization (EM) algorithm to obtain bias field estimates from the non-linear estimator of Equation 8. The EM algorithm was originally described in its general form by A.P. Dempster, N.M. Laird and D.B. Rubin in 1977 [9]. It is often used in estimation problems where some of the data is "missing." In this application, the missing data is knowledge of the tissue classes. (If they were known, then estimating the bias field would be straightforward.)

In this application, the EM algorithm iteratively alternates evaluations of the following expressions:

$$\hat{\beta} \leftarrow H(Y - WU) \tag{10}$$

$$W_{ij} \leftarrow \frac{p(\Gamma_i = \textit{tissue-class-j}) \mathrm{G}_\sigma(Y_i - \mu(\textit{tissue-class-j}) - \hat{\beta}_i)}{\sum_{\Gamma_i} p(\Gamma_i)\, \mathrm{G}_\sigma(Y_i - \mu(\Gamma_i) - \hat{\beta}_i)} \quad . \tag{11}$$

Equation 11 (the *E-Step*) is equivalent to calculating the posterior tissue class probabilities (a good indicator of tissue class) when the bias field is known. Equation 10 (the *M-Step*) is equivalent to a MAP estimator of the bias field when the tissue probabilities W are known. Thus, a good indication of tissue class is produced as a side effect of estimating the bias field. The linear operator H is applied to the difference between the measurement and a prediction based on the tissue class model.

The iteration may be started on either expression. Initial values for the weights will be needed to start with Equation 10, and initial values for the bias field will be needed to start with Equation 11.

It is shown in [9] that in many cases the EM algorithm enjoys pleasant convergence properties – namely that iterations will never worsen the value of the objective function. Provided that the bias estimates are bounded, our model satisfies the necessary conditions for guaranteed convergence.

3.2.1 Determination of the Filter H

In this section we discuss aspects of the linear filter H, its relation to the prior model on bias fields, and how it has been chosen in practice.

We have taken a Bayesian approach to estimating the bias field and tissue classes, and a formal prior model on bias fields has been assumed. One benefit of this approach is that it has allowed us to utilize the EM algorithm in this application. The prior model on the bias field is subjective in the sense described by Friden [10] (Chapter 16) – we use a subjective estimate of the unknown probability law that is implicit in the choice of filter H (Equation 9). H is related to the prior on the bias field and to the measurement noise. Ideally, H would be determined by estimating the covariance ψ_β, but given the size of this matrix, this is impractical. Instead, we examine key aspects of the ideal H and use them to select a good approximation.

H is also the optimal filter for estimating the bias when the tissue classes are known constants rather than random variables (the "complete-data" case with the EM algorithm). In this case the measurement model would be $p(Y_i \mid \beta_i) = \mathrm{G}_\sigma(Y_i - \mu(\Gamma_i) - \beta_i)$. Furthermore, H is the optimal *linear* least squares estimator (LLSE) for arbitrary models when ψ_β describes the second-order statistics of the bias field.

H is essentially equivalent to the LLSE for discrete random *processes* with given second order statistics (auto-correlation functions). Such estimators are characterized by the Wiener-Hopf equations. Applications of Wiener filtering are often approached via Fourier transforms methods, yielding a filter frequency response in terms of the power spectra of the signal and noise. The noise spectra is often known, and the signal spectra is sometimes estimated using techniques of spectral estimation. In many situations, the present complete data case included, the task is that of estimating a slowly-varying signal contaminated with white noise, and the optimal linear filter will be a low-pass filter. Lim's textbook on image processing [11] discusses this issue in Section 9.2.

In practice, it is difficult to obtain *the* optimal linear filter. H may be instead chosen as a good engineering approximation of the optimal linear filter. In this case, Equations 10 and 11 are still a useful estimator for the missing data case, and the good convergence properties of the EM algorithm still obtain. This is the approach we have taken in our implementation, where the filter was selected empirically.

Examination of the bias fields displayed in Figures 2 and 6 shows that they are slowly varying. While the low-pass filters H used in practice are unlikely to be the optimal filters for estimating bias fields, they are reasonable choices, and (some of them) correspond to reasonable estimates of the unknown probability law for bias fields. In the end, their use is justified empirically by the good results obtained via their use.

Because ψ_β is constrained to be positive semi-definite, not all choices of low-pass filter H will correspond to valid prior models on the bias field. We have found that in practice this issue is unimportant.

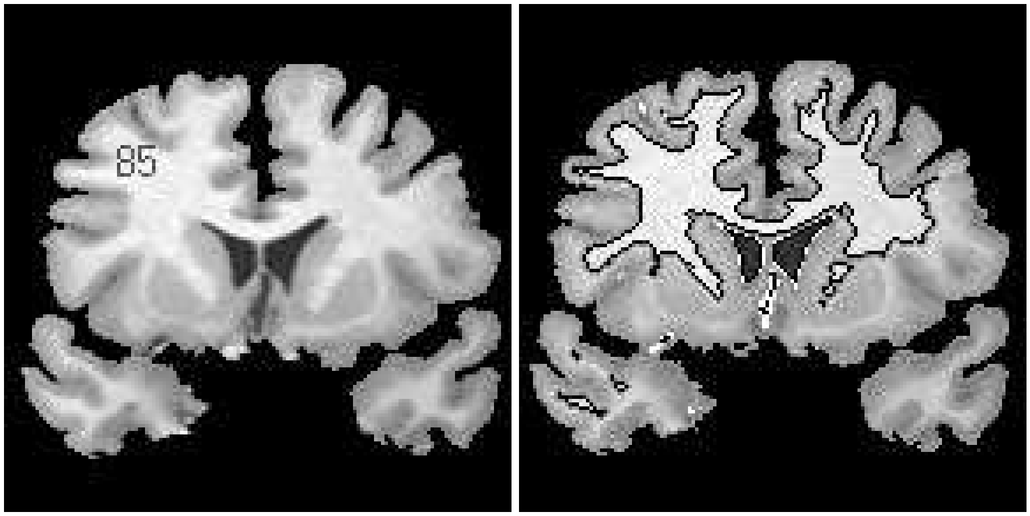

Figure 1: Original Gradient-Echo Image and Initial Segmentation

3.3 Implementation

The results described in Sections 4.1 and 4.2 were obtained using a preliminary implementation of the EM segmentation method coded in the C programming language. This single-channel, 2D implementation accommodates two tissue classes, and uses an input region of interest (ROI) to limit the part of the image to be classified and gain-corrected.

The algorithm of Section 3.2 has been initiated on the "E step", Equation 11, with a flat initial bias field, and on the "M step", Equation 10, with equal tissue class probabilities.

Iterated moving-average lowpass filters [12] have been used for the operator H in Equation 10. These filters have low computational cost that is independent of the width of their support (amount of smoothing). The filters have been adapted to only operate in the input ROI, and to adjust the effective averaging window at boundaries to confine influence to the ROI. These filters are shift-invariant, except at the boundary regions. Window widths of 11 – 15 were used. One to four filtering passes have been used with similar results. Usually, one pass is used for the sake of efficiency.

A uniform distribution was used for the prior on tissue class.

In a typical case, the program was run until the estimates stabilized, typically in 10 – 20 iterations, requiring approximately 1 second per iteration (per slice) on a Sun Microsystems Sparcstation 2.

4 RESULTS

In this section we describe the application of our approach to the segmentation of the brain into white matter and gray matter in gradient-echo and spin-echo images. Examples are shown for coronal and sagittal (surface coil) images, as well as double-echo axial images.

All of the MR images shown in this section were obtained using a General Electric Signa 1.5 Tesla clinical MR imager. An anisotropic diffusion filter developed by Gerig et al. [13] was used as a pre-processing step to reduce noise.

Operating parameters (tissue model parameters and filter parameters) were selected manually. The method has been found to be substantially insensitive to parameter settings. For a given type of acquisition, intensity variations across patients, scans, and equipment have been accommodated in the estimated bias fields without the need for manual intervention. In this sense, the method is fully automatic for segmenting healthy brain tissue.

4.1 Coronal brain examples

4.1.1 Cross Section Example

This section describes results for one slice from a coronal gradient-echo acquisition.

Figure 1 shows the input image and initial segmentation. The brain tissue ROI was generated manually. Figure 2 shows the final segmentation and bias field estimate. The largest value of the input data was 85. Note the dramatic

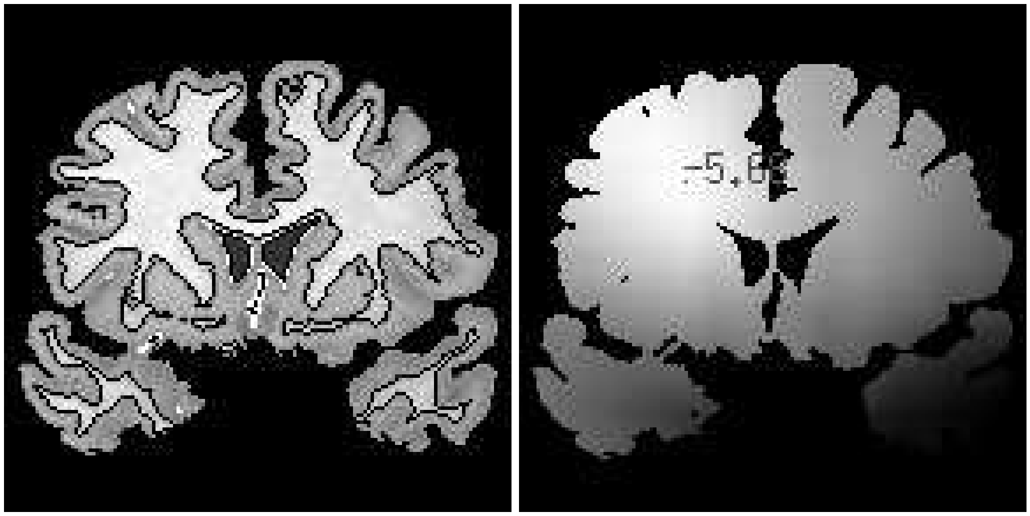

Figure 2: Final Segmentation and Bias Field

improvement in the right temporal area. In the initial segmentation the white matter is completely absent in the binarization.

4.1.2 3D Example

This section describes use of the method in the segmentation of white matter and gray matter in an entire 124 slice coronal gradient-echo data set. In Figure 3 the exterior gray matter surface of the brain is shown for reference. This surface lies just inside the brain ROI, which was generated semi-automatically as in [7].

Figure 4 shows the sub-cortical white matter surface, as determined by the EM method, while Figure 5 shows the result obtained by using the method without intensity correction, which is equivalent to conventional intensity-based segmentation. Note the generally ragged appearance and the absence of the temporal white matter structures.

The 3D renderings were generated using the dividing cubes algorithm [14].

4.2 Saggital surface coil brain example

Here we show the results of the method on a sagittal surface coil brain image. This type of data has severe intensity inhomogeneities. The five-inch receive-only surface coil was positioned at the back of the head. Figure 6 shows the intensity image, after having been windowed by a radiologist for viewing in the occipital area, and the final bias field estimate. The brain ROI was generated manually. Figure 7 shows the final binarization on the left. The right image shows a corrected intensity image. Here the gain field estimate has been applied as a correction, in the ROI. Note the dramatic improvement in “viewability” – the entire brain area is now visible, although (inevitably) the noise level is higher in the tissue that is farthest from the surface coil.

4.3 Preliminary Results – Multiple Sclerosis (MS)

This section describes preliminary results obtained for segmenting MS data. The segmenter used is a generalization of the method described in this paper that accommodates multiple tissues and two channels of data. It uses non-parametric tissue models. Figure 8 shows the input images, while Figure 9 displays initial and final segmentations. Similar results have been obtained in processing 20 complete scans for each of 50 patients, without the need for retraining or ROIs. The exams occurred over a 1.5 year period that included equipment upgrades.

5 ACCURACY ASSESSMENT

This section describes an assessment of the accuracy of the method in segmenting white matter and gray matter. Two comparisons were performed. The method was compared to manual segmentation performed by experienced

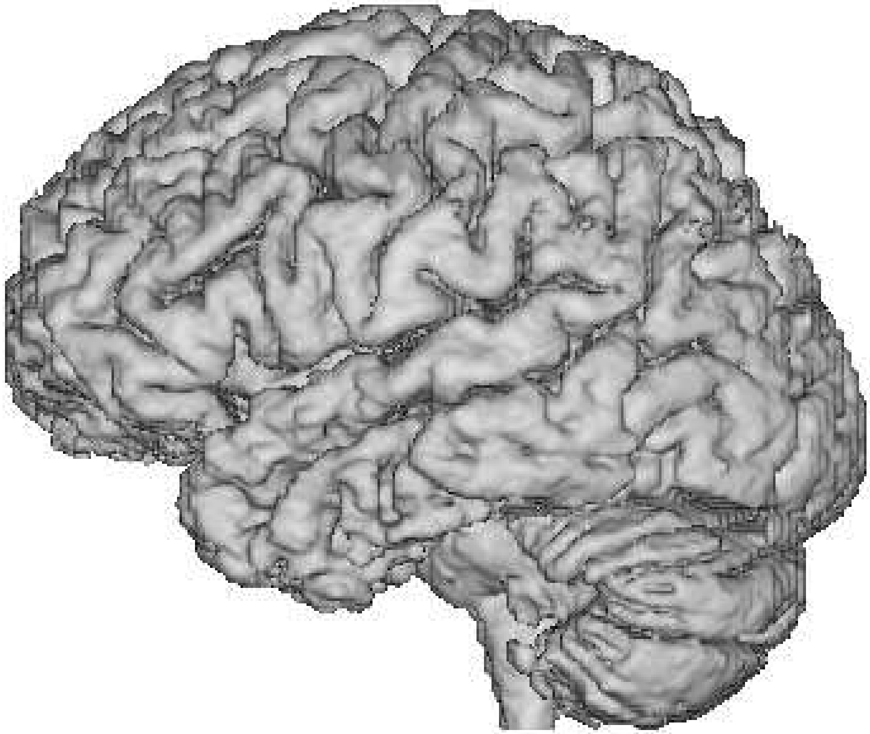

Figure 3: Gray matter surface

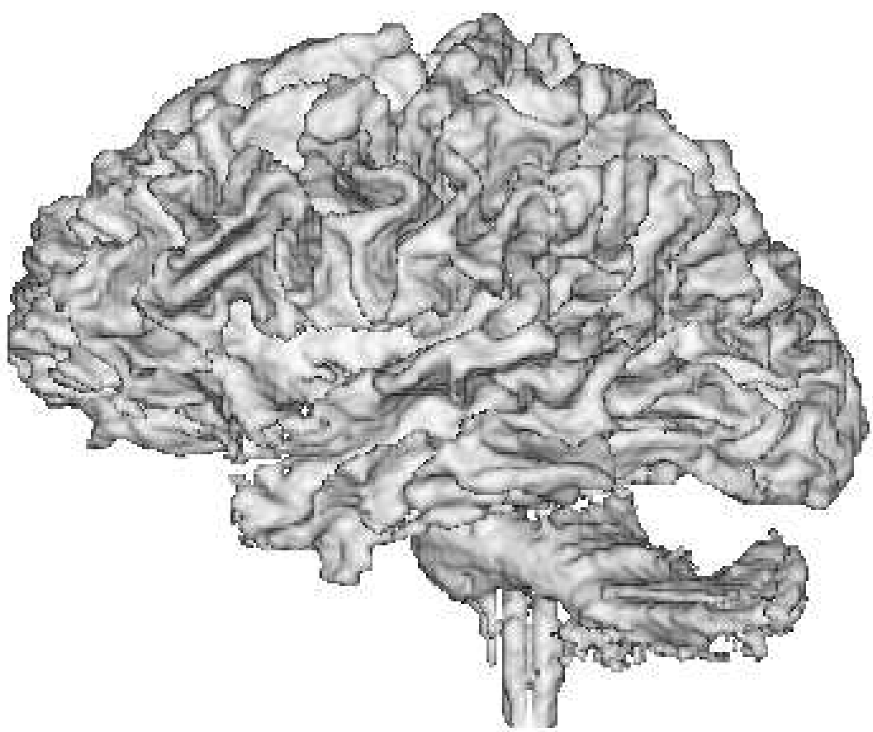

Figure 4: White Matter Surface Determined by EM Segmentation

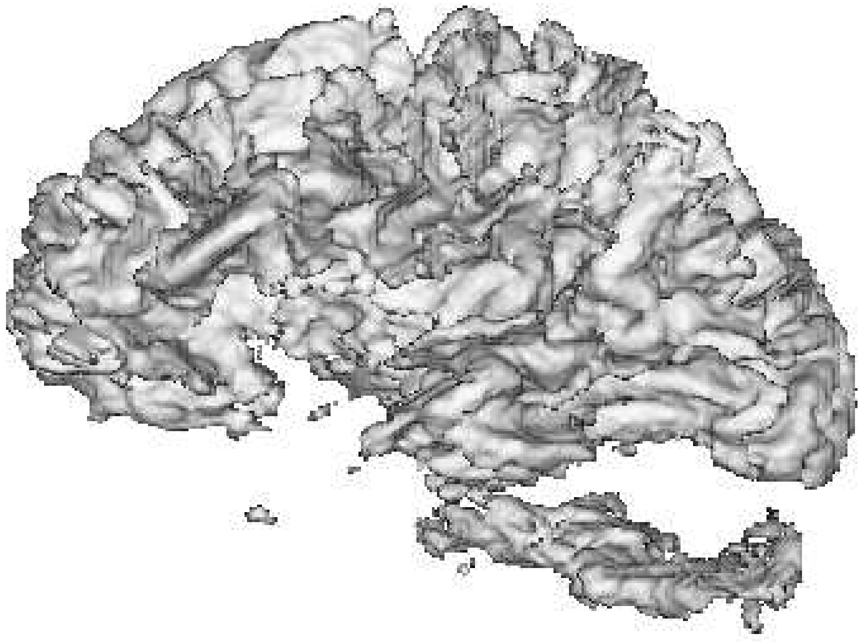

Figure 5: White Matter Surface Determined by Conventional Intensity-Based Segmentation

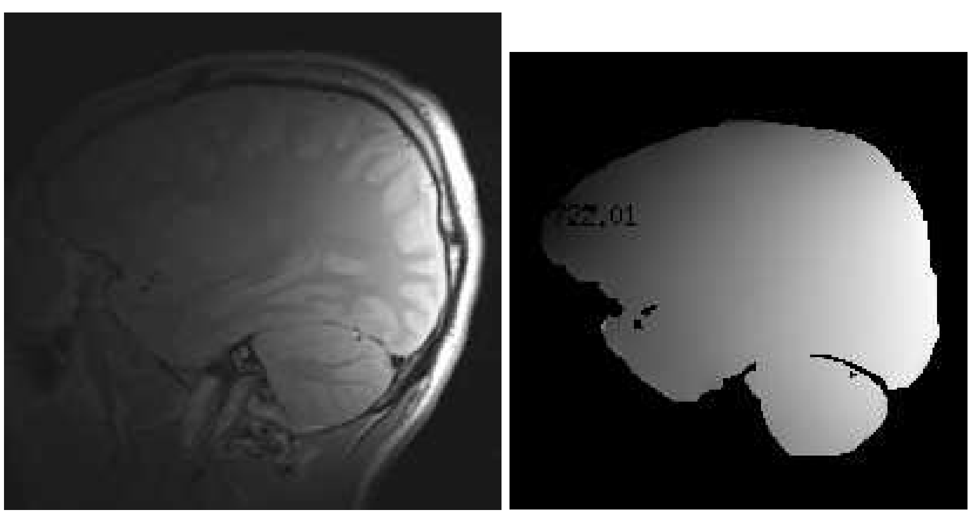

Figure 6: Intensity Image and Bias Estimate

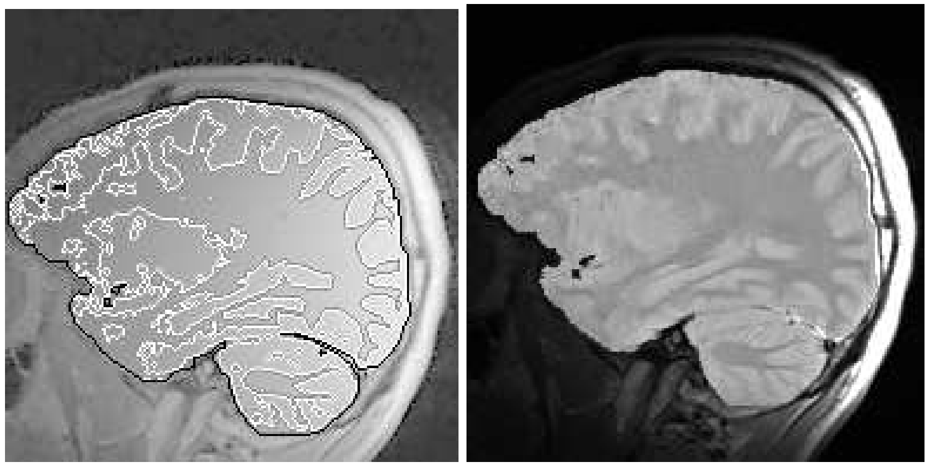

Figure 7: Segmentation and Corrected Image

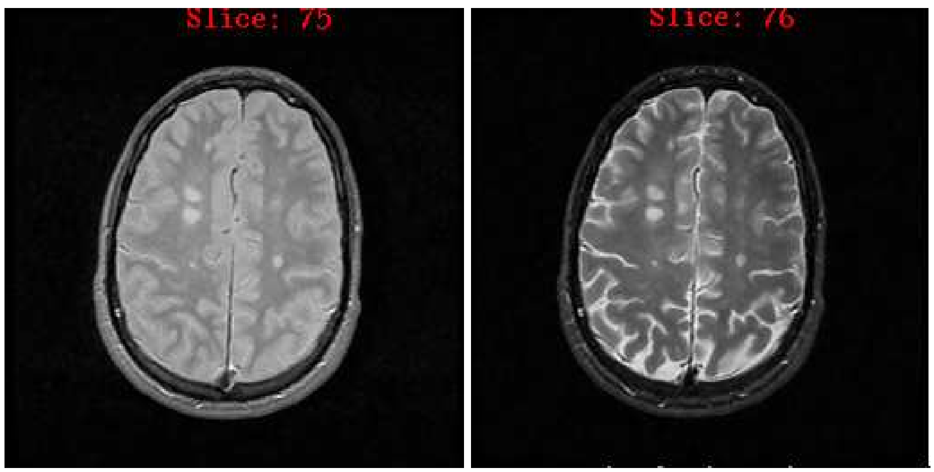

Figure 8: Multiple Sclerosis Data: Proton Density and T2-Weighted Images

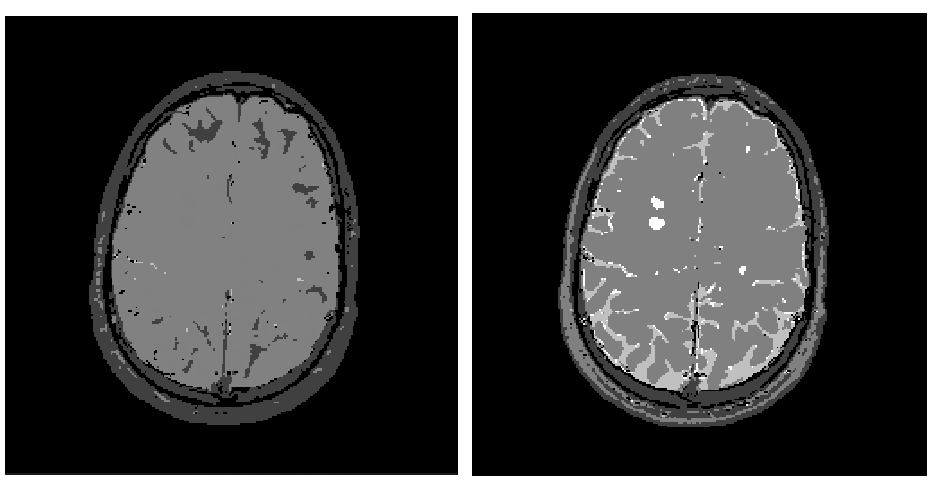

Figure 9: Initial and Final Segmentations: tissues encoded from black to white as follows: background, fat, brain tissue, CSF, plaques

	Rater A	Rater B	Rater C	Rater D	Rater E	EM Segmentation
Rater A	0.0	13.97	20.64	15.82	12.72	21.33
Rater B	13.97	0.0	22.16	15.99	15.11	20.67
Rater C	20.64	22.16	0.0	23.25	20.14	19.45
Rater D	15.82	15.99	23.25	0.0	15.30	23.02
Rater E	12.72	15.11	20.14	15.30	0.0	20.71
EM Segmentation	21.33	20.67	19.45	23.02	20.71	0.0
Average	16.90	17.58	21.13	18.58	16.80	21.04

Table 1: Percentage Differences among Manual and EM Segmentations

	Supervised Segmentation by					
Manual Segmentation by	Rater A	Rater B	Rater C	Rater D	Rater E	EM
Rater A	25.22	22.52	23.04	22.51	22.29	21.33
Rater B	23.86	21.43	21.45	21.32	20.92	20.67
Rater C	19.55	21.19	18.21	21.08	18.13	19.45
Rater D	27.45	25.68	25.78	25.47	25.08	23.02
Rater E	24.61	23.15	22.75	22.87	22.11	20.71
Average	24.15	22.79	22.25	22.65	21.71	21.04

Table 2: Percentages of Difference from Manual Segmentations of Supervised and EM Segmentations

raters, and to a method of supervised multivariate classification. The images, manual segmentations, and supervised segmentations are described in [15].

The method (EM segmentation) was applied to a single slice of an axial proton-density spin-echo brain image, using a brain-tissue ROI. The ROI was obtained by selecting those pixels that were labeled as brain tissue by four of the five raters in the manual segmentations. The amount of difference between segmentations was calculated as the percentage of pixels in the ROI having different labels.

5.1 Comparison to manual segmentation

Table 1 shows the results of comparing the method to segmentations performed manually by experienced raters. The percentage of difference within the brain ROI is shown for comparisons within a group consisting of the manual segmentations and the segmentation resulting from EM Segmentation. The lower part of the table shows the average percentage of difference from the other segmentations. The EM segmentation is consistent with the manual segmentations – it does not have the largest average difference.

5.2 Comparison to supervised classification

Table 2 shows the results of comparing the method to segmentations performed by the same expert raters using a supervised segmentation method described in [7]. In this test percentages of difference within the ROI are displayed for comparisons of the supervised segmentations and the EM segmentations with the manual segmentations described above. The average percentage of difference from the manual segmentations is also shown. The EM segmentation is seen to have less average difference from the manual segmentations than the supervised segmentations, so in this test, its performance is better.

6 DISCUSSION

Our algorithm iterates two components to convergence: estimation of tissue class probability, and gain field estimation. Our contribution has been combine them in an iterative scheme that yields a powerful new method for estimating both tissue class and gain field.

The classification component of our method is similar to the methods reported in [6] and [7]. They used Maximum-Likelihood classification of voxels using normal models with two-channel MR intensity signals. They also described a semi-automatic way of isolating the brain using connectivity.

The bias field estimation component of our method is somewhat similar to homomorphic filtering (HMF) approaches that have been reported. Lufkin et al. [16] and Axel et al. [17] describe approaches for controlling the dynamic range of surface-coil MR images. A low-pass-filtered version of the image is taken as an estimate of the gain field, and used to correct the image. Lim and Pfferbaum [18] use a similar approach to filtering that handles the boundary in a novel way, and apply intensity-based segmentation to the result.

When started on the "M Step", and run for one cycle, EM segmentation is equivalent to HMF followed by intensity-based segmentation. We have discovered, however, that more than one iteration are frequently needed to converge to good results – indicating that EM segmentation is more powerful than HMF followed by intensity-based segmentation. The essential difference is that EM segmentation uses knowledge of the tissue type to help infer the gain field. Because of this it is able to make better estimates of gain field.

Dawant, Zijdenbos and Margolin describe methods for correcting intensities for tissue classification [19]. In one variant, operator selected points of a tissue class are used to regress an intensity correction. In the other method, a preliminary segmentation is used in determining an intensity correction, which is then used for improved segmentation. This strategy is somewhat analogous to starting EM segmentation on the "E step" and running it for one and a half cycles. As in the previous case, it is plausible that better results can be obtained with additional iterations.

Several authors have reported methods based upon the use of phantoms for intensity calibration [17 20]. This approach has the drawback that the geometrical relation of the coils and the image data is not typically available with the image data (especially with surface coils). Fiducial markers were used to address this problem in [20]. In addition, the calibration approach can become complicated because the response of tissue to varying amounts of RF excitation is significantly non-linear (see [21] Equations 1-3 and 1-16). In addition, phantom calibration cannot account for possible gain inhomogeneities induced by the interaction of anatomy and the RF coils.

The correction of *magnetic* field inhomogeneities of MR images has received considerable attention. Such inhomogeneities can cause significant geometrical distortions. An effective in-vivo correction approach is described in [22].

7 EXTENSIONS

The incorporation of non-independent priors on tissue class may eliminate the need for the noise-reducing preprocessing step that is currently used.

8 CONCLUSIONS

We have demonstrated a new method, EM segmentation, for simultaneously segmenting and gain-correcting MR images.

The method increases the robustness and level of automation available for the automatic segmentation of MR images into tissue classes, thus facilitating the quantitative study of anatomical structures, such as the measurement of the volume of white and gray matter in brain structures. By improving segmentation, the approach leads to improved automatic 3D reconstruction of anatomical structures, for visualization, surgical planning and other purposes.

EM segmentation also facilitates the post-processing of medical MR images for improved appearance by correcting the RF gain variations apparent in the image. This is especially useful for images derived from surface coils, where the large gain variations make it difficult to accommodate the image data on films for viewing.

9 ACKNOWLEDGMENTS

We thank Maureen Ainsle, Ihan Chou, Steve Hushek, Hiroto Hokama, Martha Shenton and Cynthia Wible for providing test cases and evaluating our method. Sanjeev Kulkarni provided valuable comments on an early draft of this paper.

10 REFERENCES

[1] M. Shenton, R. Kikinis, F. Jolesz, et al. Abnormalities of the Left Temporal Lobe and Thought Disorder in Schizophrenia. *N. Engl. J. Med.*, (327):604–612, 1992.

[2] K. Höhne et al. A framework for the Generation of 3D Anatomical Atlases. In *SPIE Vol. 1808, Visualization in Biomedical Computing 1992*, 1992.

[3] R. Kikinis, F.A. Jolesz, W.E. Lorensen, H.E. Cline, P.E Stieg, and P. McL. Black. 3d Reconstruction of Skull Base Tumors from MRI Data for Neurosurgical Planning. In *Proceedings of the Society of Magnetic Resonance in Medicine Conference*, 1991.

[4] M Vannier, R Butterfield, D Jordan, and W Murphy et al. Multi-Spectral Analysis of Magnetic Resonance Images. *Radiology*, (154):221 – 224, 1985.

[5] M. Kohn, N. Tanna, G. Herman, et al. Analysis of Brain and Cerebrospinal Fluid Volumes with MR Imaging. *Radiology*, (178):115 – 122, 1991.

[6] G. Gerig, W. Kuoni, R. Kikinis, and O. Kübler. Medical Imaging and Computer Vision: an Integrated Approach for Diagnosis and Planning. In *Proc. 11'th DAGM Symposium*, pages 425–443. Springer, 1989.

[7] H.E. Cline, W.E. Lorensen, R. Kikinis, and F. Jolesz. Three-Dimensional Segmentation of MR Images of the Head Using Probability and Connectivity. *JCAT*, 14(6):1037–1045, 1990.

[8] M. Kamber, D. Collins, R. Shinghal, G. Francis, and A. Evans. Model-Based 3D Segmentation of Multiple Sclerosis Lesions in Dual-Echo MRI Data. In *SPIE Vol. 1808, Visualization in Biomedical Computing 1992*, 1992.

[9] A.P. Dempster, N.M. Laird, and D.B. Rubin. Maximum Likelihood from Incomplete Data via the EM Algorithm. *J. Roy. Statist. Soc.*, 39:1 – 38, 1977.

[10] B.R. Frieden. *Probability, Statistical Optics, and Data Testing*. Springer-Verlag, 1983.

[11] J.S. Lim. *Two-Dimensional Signal and Image Processing*. Prentice Hall, 1990.

[12] W.M. Wells III. Efficient Synthesis of Gaussian Filters by Cascaded Uniform Filters. *IEEE Transactions PAMI*, PAMI-8(2):234 – 239, March 1986.

[13] G. Gerig, O. Kübler, and F. Jolesz. Nonlinear Anisotropic Filtering of MRI data. *IEEE Trans. Med. Imaging*, (11):221–232, 1992.

[14] H. Cline, W. Lorensen, S. Ludke, C. Crawford, and B. Teeter. Two Algorithms for the Three-Dimensional Reconstruction of Tomograms. *Med. Phys.*, (15):320 – 327, 1988.

[15] R. Kikinis, M. Shenton, F.A. Jolesz, G. Gerig, J. Martin, M. Anderson, D. Metcalf, C. Guttmann, R.W. McCarley, W. Lorensen, and H. Cline. Quantitative Analysis of Brain and Cerebrospinal Fluid Spaces with MR Imaging. *JMRI*, 2:619–629, 1992.

[16] R.B. Lufkin, T. Sharpless, B. Flannigan, and W. Hanafee. Dynamic-Range Compression in Surface-Coil MRI. *AJR*, 147(379):379–382, 1986.

[17] L. Axel, J. Costantini, and J. Listerud. Intensity Correction in Surface-Coil MR Imaging. *AJR*, 148(4):418–420, 1987.

[18] K.O. Lim and A. Pfferbaum. Segmentation of MR Brain Images into Cerebrospinal Fluid Spaces, White and Gray Matter. *JCAT*, 13(4):588–593, 1989.

[19] B. Dawant, A. Zijdenbos, and R. Margolin. Correction of Intensity Variations in MR Images for Computer-Aided Tissue Classification. *IEEE Trans. Med. Imaging*, 12(4):770 – 781, 1993.

[20] J. Gohagan, E. Spitznagel, W. Murphy, M. Vannier, et al. Multispectral Analysis of MR Images of the Breast. *Radiology*, (163):703 – 707, 1987.

[21] D. Stark and Jr. W. Bradley, editors. *Magnetic Resonance Imaging*. Mosby Year Book, 1990.

[22] E. Schneider and G.H. Glover. Rapid In-Vivo Proton Shimming. *Magn. Resonance in Med.*, 18:335–347, 1991.